

A six-part collisional model of the main asteroid belt

H. Cibulková, M. Brož

Institute of Astronomy, Charles University in Prague, V Holešovičkách 2, 18000 Prague 8, Czech Republic, e-mail: H333@seznam.cz, mira@sirrah.troja.mff.cuni.cz

P. G. Benavidez

Departamento de Física, Ingeniería de Sistemas y Teoría de la Señal, Universidad de Alicante, P.O. Box 99, 03080 Alicante, Spain, e-mail: paula.benavidez@ua.es

Abstract

In this work, we construct a new model for the collisional evolution of the main asteroid belt. Our goals are to test the scaling law of Benz and Asphaug (1999) and ascertain if it can be used for the whole belt. We want to find initial size-frequency distributions (SFDs) for the considered six parts of the belt (inner, middle, ‘pristine’, outer, Cybele zone, high-inclination region), and to verify if the number of asteroid families created during the simulation matches the number of observed families as well. We used new observational data from the WISE satellite (Masiero et al., 2011) to construct the observed SFDs. We simulate mutual collisions of asteroids with a modified version of the Boulder code (Morbidelli et al., 2009), where the results of hydrodynamic (SPH) simulations of Durda et al. (2007) and Benavidez et al. (2012) are included. Because material characteristics can significantly affect breakups, we created two models — for monolithic asteroids and for rubble-piles. To explain the observed SFDs in the size range $D = 1$ to 10 km we have to also account for dynamical depletion due to the Yarkovsky effect. The assumption of (purely) rubble-pile asteroids leads to a significantly worse fit to the observed data, so that we can conclude that majority of main-belt asteroids are rather monolithic. Our work may also serve as a motivation for further SPH simulations of disruptions of smaller targets (with a parent body size of the order of 1 km).

Keywords: main asteroid belt; collisions; size-frequency distribution; asteroid families

1. Introduction

The collisional evolution of the main asteroid belt is studied for more than 60 years (Dohnanyi (1969), Davis et al. (1979) etc.). The first collisional model was created by Dohnanyi (1969) and its important result was that the final slope of the cumulative size-frequency distribution for asteroids in a collisional equilibrium will be close to -2.5 . An overview of previous modelling of the main belt and subsequent advances can be found in a relatively recent paper by Bottke et al. (2005), so that we shall not repeat it here. Nevertheless, it worth to mention another development, which is an attempt to merge a classical particle-in-a-box collisional model with (parametric) results of smooth-particle hydrodynamic (SPH) codes as done in Morbidelli et al. (2009). **We are going to use this kind of method in this work.**

Every collisional model should comply with two important constraints: 1) the size-frequency distribution (SFD) of main belt at the end of a simulation must fit the observed SFD; 2) the number of asteroid families created during this simulation must fit the observed number of families. It is important to note, that the models were improved in the course of time not only due to the progress of technology or new methods but also thanks to an increasing amount of observational data. In this work, we could exploit new data obtained by the WISE satellite (Wide-field Infrared Survey Explorer; Masiero et al., 2011), specifi-

cally, diameters and geometric albedos for 129,750 asteroids.

Moreover, several tens of asteroid families are observed in the main belt as shown by many authors (Zappalà et al., 1995; Nesvorný et al., 2005; Nesvorný, 2010; Brož et al., 2013; Masiero et al., 2013). The lists of collisional families are also steadily improved, they become more complete and (luckily) compatible with each other.

In order to fully exploit all new data, we created a new collisional model in which we divided the whole main belt to six parts (see Section 2 for a detailed discussion and Section 3 for the description of observational data). Our **aims** are: 1) to check the number of families in individual parts of the belt — we use the list of families from Brož et al. (2013) (which includes also their physical properties) with a few modifications; 2) to verify if a single scaling law (e.g. Benz and Asphaug, 1999) can be used to fit the *whole* asteroid belt, or it is necessary to use two different scaling laws, e.g. one for the inner belt and second for the outer belt; 3) and we also test a hypothesis, if the main belt is mostly composed of monolithic or rubble-pile objects.

In this paper, we assume that all families observed today were created in the last ~ 4 Gyr (without any influence of the late heavy bombardment dated approximately 4.2 to

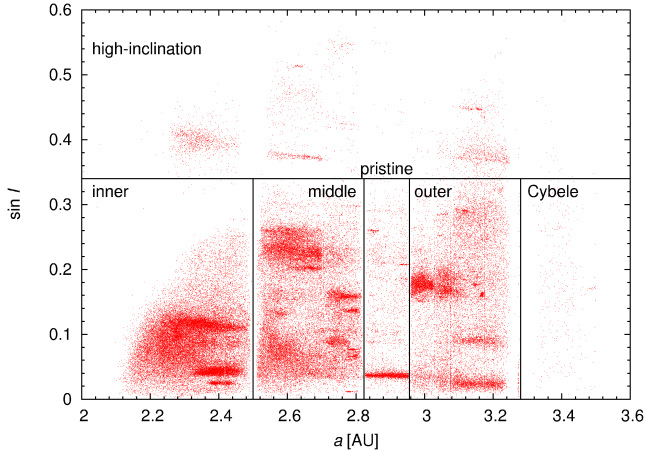


Figure 1: A definition of the six parts of the main asteroids belt according to the semimajor axis a and the inclination I : inner, middle, ‘pristine’, outer, Cybele zone and high-inclination region.

3.85 Gyr ago).¹ We thus focus on an almost steady-state evolution of the main belt, without any significant changes of collisional probabilities or dynamical characteristics. This is different from the work of Bottke et al. (2005).

We model collisions with the statistical code called Boulder (Morbidelli et al., 2009) that we slightly extended to account for six populations of asteroids (Sections 5, 6). As mentioned above, the Boulder code incorporates the results of the SPH simulations by Durda et al. (2007) for *monolithic* $D_{PB} = 100$ km parent bodies, namely for the masses of the largest remnant and fragment and an overall slope of fragment’s SFD. For asteroids larger or smaller than $D_{PB} = 100$ km a simple scaling is used.

Material characteristics definitely have significant influence on mutual collisions (e. g. Michel et al., 2011; Benavidez et al., 2012). Therefore, we also run simulations with *rubble-pile* objects, which are less firm (refer to Section 7). A set of simulations analogous to Durda et al. (2007) for rubble-pile targets with $D_{PB} = 100$ km was computed by Benavidez et al. (2012).

First, we try to explore the parameter space using a simplex algorithm while we keep the scaling law fixed. Considering a large number of free parameters and the stochasticity of the system, we look only for some local minima of χ^2 and we do not expect to find a statistically significant global minimum. Further possible improvements and extensions of our model are discussed in Sections 8 and 9.

2. A definition of the six parts of the main belt

We divided the main belt to six parts (sub-populations) according to the orbital elements (the semimajor axis a and the inclination I , Figure 1). Five parts separated by major mean-motion

¹This is an approach different from Brož et al. (2013), where (at most) 5 large ($D_{PB} > 200$ km) catastrophic disruptions were attributed to the LHB. Nevertheless, there was a possibility (at a few percent level) that all the families were created without the LHB. So our assumptions here do not contradict Brož et al. (2013) and we will indeed discuss a possibility that the number of post-LHB families is lower than our ‘nominal’ value.

resonances with Jupiter are well-defined — if an asteroid enters the resonance due to the Yarkovsky effect (Bottke et al., 2006), its eccentricity increases and the asteroid becomes a near-Earth object. Consequently, **vast majority of large** asteroids do not cross the resonances² **and we do not account for resonance crossing in our model**. The sixth part is formed by asteroids with high inclinations, $\sin I_p > 0.34$. This value corresponds approximately to the position of the ν_6 secular resonance.

Namely, the individual parts are defined as follows:

1. inner belt – from $a = 2.1$ to 2.5 AU (i.e. the resonance 3:1);
2. middle belt – from 2.5 to 2.823 AU (5:2);
3. ‘pristine’ belt – from 2.823 to 2.956 AU (7:3);
4. outer belt – from 2.956 to 3.28 AU (2:1);
5. Cybele zone – from 3.3 to 3.51 AU;
6. high-inclination region – $\sin I > 0.34$.

For a and $\sin I$ we preferentially used the proper values from the AstDyS catalogue (Asteroids Dynamic Site; Knežević and Milani, 2003)³. For remaining asteroids, not included in AstDyS, we used osculating orbital elements from the AstOrb catalogue (The Asteroid Orbital Elements Database)⁴.

3. Observed size-frequency distributions

To construct SFDs we used the observational data from the WISE satellite (Masiero et al., 2011)⁵. For asteroids not included there we could exploit the AstOrb catalogue (i.e. data from IRAS; Tedesco et al., 2002). For remaining asteroids, we calculated their diameters according the relation (Bowell et al., 1989)

$$D = 10^{0.5(6.259 - \log p_V) - 0.4H}, \quad (1)$$

where H denotes the absolute magnitude from the AstOrb catalogue and p_V the (assumed) geometric albedo. **We assigned albedos to asteroids without a known diameter** randomly, by a Monte-Carlo method, from the distributions of albedos constructed according to the WISE data. For each part of the main belt, we constructed a distribution of albedos separately. The resulting observed SFDs are shown in Figure 2. We can see clearly that the individual SFDs differ significantly in terms slopes and total numbers of asteroids.

To verify a validity of this method, we perform the following test (for the whole main belt). We assume a known set of diameters. We then assign albedos randomly to the individual diameters according to the distribution of WISE albedos. We

²For very small asteroids ($D \lesssim 10$ m) we must be more careful. Nevertheless, if an asteroid is able to cross the resonance between e.g. the pristine and the middle belt (i.e. increasing the population of the middle belt) then another asteroid is able to cross the resonance between the middle and the inner belt (decreasing the population of the middle belt). The crossing of the resonances essentially corresponds to a longer time scale of the dynamical decay, which we shall discuss in Section 8.

³<http://hamilton.dm.unipi.it/astdys/>

⁴<ftp://ftp.lowell.edu/pub/elgb/astorb.html>

⁵http://wise2.ipac.caltech.edu/staff/bauer/NEOWISE_pass1/

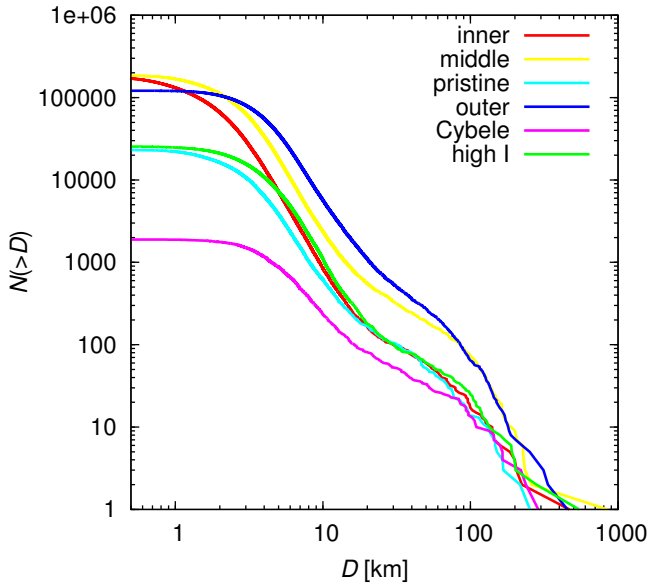


Figure 2: The observed cumulative size-frequency distributions $N(>D)$ of the six parts of the main belt. We used the observational data from the WISE satellite (Masiero et al., 2011) and the AstOrb catalogue for their construction. For asteroids which have no albedos in the WISE database, we assigned albedos by a Monte Carlo method from the distribution of WISE albedos.

calculate the values of the absolute magnitudes H by the inversion of Eq. (1). Now, we try to reconstruct the SFD from H and p_V . The new "unknown" values of diameters are computed according Eq. (1) and for the values of p_V we test three following options: 1) a fixed albedo $p_V = 0.15$; 2) the mean value $p_V = 0.13$ (derived from the distribution of WISE albedos); 3) for $H < 15$ mag we used the known albedos, for other bodies we assigned albedos by the Monte-Carlo method as above. The known SFD and the three reconstructed SFDs are shown in Figure 3.

The largest uncertainties of the reconstruction are given by the method of assignment of geometric albedos, but we verified that the third method is the best one and that these uncertainties are much smaller than the differences between individual SFDs as seen in Figure 2.

Another possible difficulty, especially for asteroids with diameters $D < 10$ km, is the observational bias. In Figure 2, we can see that for sizes smaller than some D_{complete} the total number of asteroids remains constant. **We also probably miss same asteroids with $D_{\text{complete}} < D < 10$ km.** These objects are less bright than the reach of current surveys: LINEAR (Stuart, 2001), Catalina⁶, Spacewatch (Bottke et al., 2002), or Pan-STARRS (Hodapp et al., 2004). Nevertheless, for $D > 10$ km we need not to perform debiasing and neither for smaller asteroids we do not account for the bias, because the range of diameters D where we fit our model is limited (see Table 4).

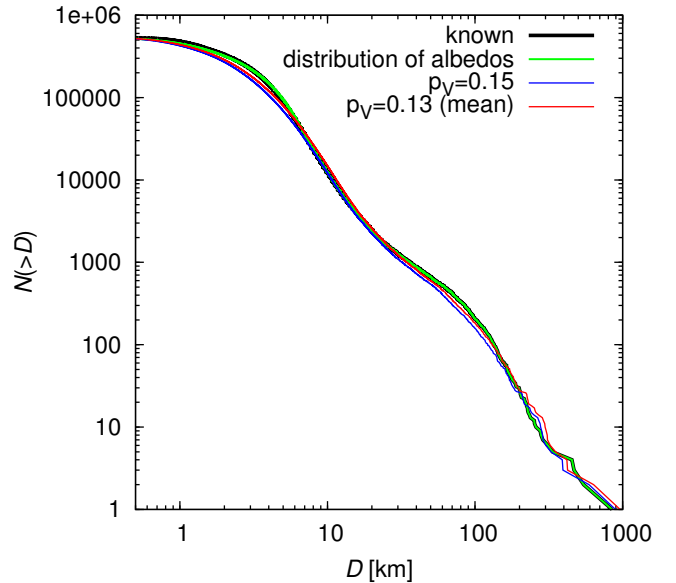


Figure 3: A test of three reconstructions of a "known" SFD. Diameters were calculated according to Eq. 1 and for values of p_V we try to use: 1) $p_V = 0.15$ (blue line), 2) $p_V = 0.13$, i.e. the mean value from the distribution of WISE albedos (red line), and 3) we used albedos from WISE for $H < 15$ mag; for other bodies we assigned albedos by a Monte-Carlo method according to the distribution of WISE albedos (green line). We can see that the third method is the best one.

4. Collisional probabilities and impact velocities

To model the collisional evolution of the main belt by the Boulder code we need to know the intrinsic probabilities p_i of collisions between individual parts and the mutual impact velocities v_{imp} . The values of p_i and v_{imp} were computed by the code written by W.F. Bottke (Bottke and Greenberg, 1993; Greenberg, 1982).

We calculated p_i 's and v_{imp} 's between each pair of asteroids of different populations. We used first 1,000 asteroids from each population (first according to the catalogue nomenclature). We checked that this selection does not significantly influence the result. From these sets, we computed the mean values \bar{p}_i , \bar{v}_{imp} (for v_{imp} only if $p_i \neq 0$). We checked that the distributions are relatively close to the Gauss distribution and the computations of the mean values are reasonable.

We found out that the individual p_i and v_{imp} differ significantly (values from 0.35×10^{-18} to $11.98 \times 10^{-18} \text{ km}^{-2} \text{ yr}^{-1}$ and from 2.22 to 10.09 km s^{-1}) — see Table 1. The collision probability decreases with an increasing difference between semimajor axis of two asteroids (the lowest value is for the interaction between the inner belt and the Cybele zone, while the highest for the interactions inside the inner belt). The highest impact velocities are for interactions between the high-inclination region and any other population.

The uncertainties of \bar{p}_i are of the order $0.1 \times 10^{-18} \text{ km}^{-2} \text{ yr}^{-1}$ and for \bar{v}_{imp} 0.1 km s^{-1} . Values computed by Dahlgren (1998), $p_i = 3.1 \times 10^{-18} \text{ km}^{-2} \text{ yr}^{-1}$ and $v_{\text{imp}} = 5.28 \text{ km s}^{-1}$ (mean values for the whole main belt), are in accordance with our results. However, it seems to be clear that considering only a single

⁶<http://www.lpl.arizona.edu/css/>

Table 1: The computed mutual impact velocities \bar{v}_{imp} and the intrinsic collisional probabilities \bar{p}_i between individual parts of the main asteroid belt.

interacting populations	\bar{p}_i ($10^{-18} \text{ km}^{-2} \text{ yr}^{-1}$)	\bar{v}_{imp} (km s^{-1})
inner – inner	11.98	4.34
inner – middle	5.35	4.97
inner – pristine	2.70	3.81
inner – outer	1.38	4.66
inner – Cybele	0.35	6.77
inner – high inc.	2.93	9.55
middle – middle	4.91	5.18
middle – pristine	4.67	3.96
middle – outer	2.88	4.73
middle – Cybele	1.04	5.33
middle – high inc.	2.68	8.84
pristine – pristine	8.97	2.22
pristine – outer	4.80	3.59
pristine – Cybele	1.37	4.57
pristine – high inc.	2.45	7.93
outer – outer	3.57	4.34
outer – Cybele	2.27	4.45
outer – high inc.	1.81	8.04
Cybele – Cybele	2.58	4.39
Cybele – high inc.	0.98	7.87
high inc. – high inc.	2.92	10.09

value of p_i and v_{imp} for the *whole* main belt would result in an systematic error of the model.

5. A construction of the model

In this Section, we are going to describe free and fixed input parameters of our model and the principle how we explore the parameter space.

The initial SFDs of the six parts of the main belt are described by 36 free parameters — six for every part: q_a, q_b, q_c, d_1, d_2 and n_{norm} . Parameter q_a denotes the slope of the SFD for asteroids with diameters $D > d_1$, q_b the slope between d_1 and d_2 , q_c the slope for $D < d_2$ and n_{norm} is the normalization of the SFD at d_1 .

We must also “manually” add biggest asteroids, which likely stay untouched from their formation, to the input SFDs: (4) Vesta with a diameter 468.3 km (according to AstOrb) in the inner belt, (1) Ceres with a diameter 848.4 km (AstOrb) in the middle belt, and (2) Pallas with a diameter 544 km (Masiero et al., 2011) in the high-inclination region. These asteroids are too big and “solitary” in the respective part of the SFD and consequently cannot be described by the slope q_a .

The list of fixed input parameters follows: collision probabilities and impact velocities from Section 4; the scaling law parameters according to Benz and Asphaug (1999); initial (–4 Gyr) and final (0) time and the time step (10 Myr).

5.1. The scaling law

One of the input parameters is the scaling law described by a parametric relation

$$Q_D^* = \frac{1}{q_{\text{fact}}} (Q_0 r^a + B \rho r^b), \quad (2)$$

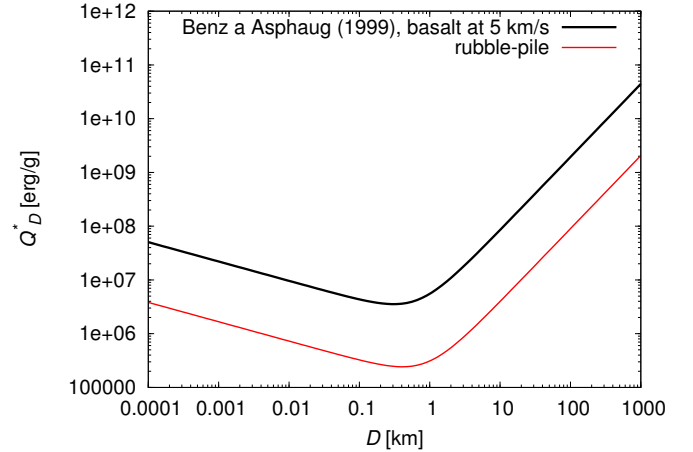


Figure 4: The scaling law for basaltic material at 5 km/s (black line). The red line represents the scaling law for rubble-pile bodies, with which we work in Section 7.

where r denotes the radius in cm, ρ the density in g/cm^3 . Q_D^* is the specific impact energy required to disperse half of the total mass of a target. A scaling law which is often used is that of Benz and Asphaug (1999) (Figure 4), which was derived on the basis of SPH simulations. Parameters in Eq. 2, corresponding to Benz and Asphaug (1999), are listed in Table 2.

5.2. A definition of the χ^2 metric

To measure a match between our simulations and the observations we calculate χ^2 prescribed by the relation

$$\chi^2 = \sum_{i=1}^n \frac{(\text{syn}_i - \text{obs}_i)^2}{\sigma_i^2}, \quad (3)$$

where syn_i denotes the synthetic data (i.e. results from Boulder simulations) and obs_i denotes the observed data, σ_i is the uncertainty of the corresponding obs_i . The quantities syn_i and obs_i are namely the cumulative SFDs $N(>D)$ or the numbers of families N_{families} . More exactly, we calculate χ_{std}^2 firstly for 96 points in the cumulative SFDs of the six populations and we add χ_{fam}^2 for the numbers of families in these populations. To minimize χ^2 we use a simplex numerical method Press et al. (1992).

The χ^2 prescribed by Eq. (3) is clearly not a “classical” χ^2 , but a “pseudo”- χ^2 , because we do not have a well-determined σ_i .⁷ Using χ^2 we can only decide, if our model corresponds to the observations within the prescribed uncertainties σ_i . Specifically, we used $\sigma_i = 10\% \text{ obs}_i$ for the SFDs (similarly as Botke et al., 2005) and $\sigma_i = \sqrt{\text{obs}_i}$ for the families.⁸

⁷We cannot use a usual condition $\chi^2 \approx n$ or the probability function $q(\chi^2|n)$ to assess a statistical significance of the match between the synthetic and observed data.

⁸We prefer to use cumulative values $N(>D)$ instead of differential, even though the bins are not independent of each other. The reason is more-or-less technical: the Boulder code can create new bins (or merge existing bins) in the course of simulation and this would create a numerical artefact in the χ^2 computation.

Table 2: Parameters of the scaling law according to Benz and Asphaug (1999) (see Eq. 2). Parameters q_{fact} , Q_0 and B are the normalization parameters, a and b characterize the slope of the corresponding power law. **The procedure how we obtained the parameters for rubble-pile bodies is described in Section 7.1.**

	ρ (g/cm ³)	Q_0 (erg/g)	a	B (erg/g)	b	q_{fact}
basalt	3.0	9×10^7	-0.36	0.5	1.36	1.0
rubble-pile	1.84	9×10^7	-0.36	0.5	1.36	13.2

Table 3: The list of asteroid families in individual parts of the main belt according to Brož et al. (2013) and Walsh et al. (2013). Only families with the diameter of the parent body $D_{\text{PB}} > 100$ km and the ratio of the largest remnant/fragment to the parent body $M_{\text{LF}}/M_{\text{PB}} < 0.5$ are listed.

belt	N_{fam}	families		
inner	3	Erigone	Eulalia	New Polana
middle	8	Maria	Padua	Misa
		Dora	Merxia	Teutonia
pristine	2	Gefion	Hoffmeister	
		Koronis	Fringilla	
outer	6	Themis	Meliboea	Eos
		Ursula	Veritas	Lixiaohua
high inc.	1	Alauda		

Six values of χ_{fam}^2 would have only small influence on the total χ^2 . Therefore, we used a weighting for families, $w_{\text{fam}} = 10$, because the numbers of families are important indicators for us. Different numbers of synthetic families would mean, besides other things, a different structure of the main belt in the space of proper orbital elements.

We focused on families with **the diameter of the parent body $D_{\text{PB}} \geq 100$ km and the ratio of the largest remnant/fragment to the parent body $D_{\text{LF}}/D_{\text{PB}} < 0.5$ only (i.e. catastrophic disruptions), though the Boulder code treats also cratering events, of course.** The numbers of observed families N_{fam} in individual parts are taken from Brož et al. (2013), except for the inner belt, where two additional families were found by Walsh et al. (2013) (i.e. three families in total, see Table 3).

In order to avoid complicated computations of the observational bias we simply limit a range of the diameters D_1 to D_2 where χ^2 is computed (see Table 4) **and we admit a possibility that χ^2 is slightly increased for D approaching D_2 . We estimated D_1 and D_2 for each population separately from the observed SFDs shown in Figure 2.**

6. Simulations for monolithic objects

We can expect a different evolution of individual populations as a consequence of their different SFDs, collision probabilities and impact velocities. Therefore, in this Section we are going to run simulations with a new collisional model with six populations.

6.1. An analysis of an extended parameter space

First, we explored the parameter space on larger scales and started the simplex with many different initial conditions (see

Table 5: The changes of input parameters between cycles and steps of the simplex within one cycle. d_1 , d_2 , q_a , q_b , q_c and n_{norm} denote the same parameters as in Table 4. For the middle and outer belt, which are more populous, we used $\Delta n_{\text{norm}} = 15$ and $\delta n_{\text{norm}} = 5$.

	d_1 (km)	d_2 (km)	q_a	q_b	q_c	n_{norm}
cycles	± 15	± 6	± 0.3	± 0.6	± 0.6	$\pm 6; 15$
steps	5	2	0.1	0.2	0.2	2; 5

Figure 5). The calculation had 36 free parameters, as explained above. To reduce the total computational time, we change the same parameter in each part of the main belt with every initialisation of the simplex. **For example, we increase all parameters q_{a1} , q_{a2} , q_{a3} , q_{a4} , q_{a5} , q_{a6} together and then we search for a neighbouring local minimum with the simplex which has all 36 parameters free** — we call this one cycle. In total, we run $3^6 = 729$ cycles (i.e. initialisations of the simplex), **for each parameter we examined 3 values (the input value from Table 4 and two surrounding values — as described in Table 5).** The maximum permitted number of iterations of the simplex was 300 in one cycle (and we verified that this is sufficient to find a χ^2 value which is already close to local minimum). In total, we run 218,700 simulations of the collisional evolution of the main belt.

The input parameters are summarised in Table 4, while the changes of parameters between cycles and the steps of simplex within one cycle are listed in Table 5.

The minimum value of χ^2 , which we obtained, is $\chi^2 = 562$, but we found many other values, that are statistically equivalent (see Figure 6 as an example). Therefore, we did not find a statistically significant global minimum. The parameters q_{b1-b6} seem to be well-determined within the parameter space, parameters q_{a1-a6} , d_{1-6} , d_{2-6} and $n_{\text{norm}1-6}$ are slightly less constrained. For the remaining parameters q_{c1-c6} we essentially cannot determine the best values. This is caused by the fact that the ‘tail’ of the SFD is created easily during disruptions of larger asteroids, so that initial conditions do not matter.

The differences between simulated and observed SFDs and numbers of families for individual populations corresponding to $\chi^2 = 562$ are shown in Figures 7 and 8. We can see that the largest differences are for the inner and outer belt. Note that it is *not* easy to improve these results, e.g. by increasing the normalization $n_{\text{norm}4}$ of the outer belt, because this would affect all of the remaining populations too.

The parameters of the initial SFDs for the minimal χ^2 are summarised in Table 6. Comparing with Table 4, the

Table 4: The input parameters describing the SFDs of the six parts of the main belt: q_a denotes the slope of the SFD for asteroids with diameters $D > d_1$, q_b the slope between d_1 and d_2 , q_c the slope for $D < d_2$ and n_{norm} is the normalization of the SFD at d_1 . N_{fam} denotes the number of observed families and D_1 and D_2 the range of diameters in the SFD, where the χ^2 is calculated.

population	d_1 (km)	d_2 (km)	q_a	q_b	q_c	n_{norm}	N_{fam}	D_1 (km)	D_2 (km)
inner	90	20	-3.9	-2.1	-3.6	20	3	250	3
middle	105	18	-4.3	-2.3	-3.6	75	8	250	3
pristine	100	13	-3.6	-2.4	-3.6	21	2	250	5
outer	80	20	-3.7	-2.5	-3.5	90	6	250	5
Cybele	80	15	-2.5	-2.0	-2.8	17	0	250	6
high-inclination	100	20	-3.9	-2.2	-3.5	30	1	250	5

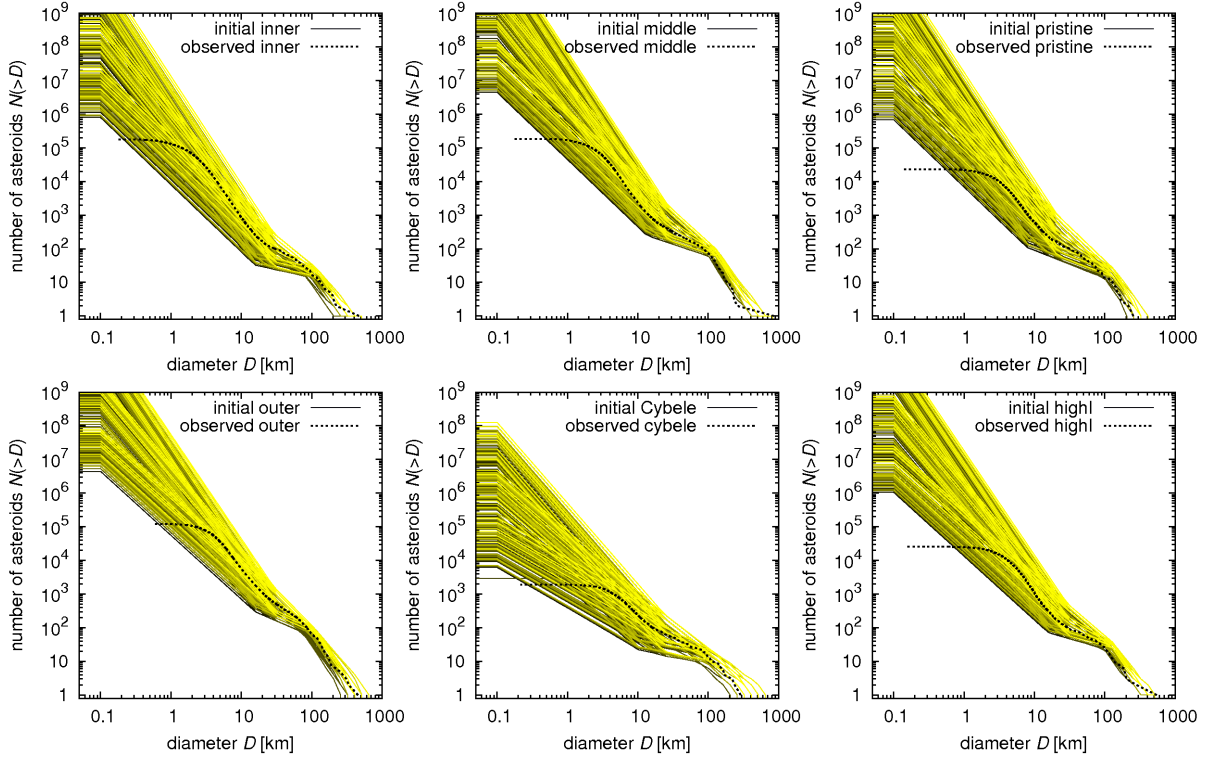


Figure 5: A set of 729 synthetic size-frequency distributions (for six parts of the main belt), which served as starting points for the simplex algorithm and subsequent simulations of collisional evolution. Thin lines (with various colours) denote the synthetic SFD's, while the thick lines corresponds to the observed SFDs. Note that we tested quite a large range of possible initial conditions. The number of simplex steps was limited to 300 because the convergence to a local minimum is difficult due to the stochasticity of the collisional evolution. The total number of collisional simulations we ran was thus $729 \times 300 = 218,700$.

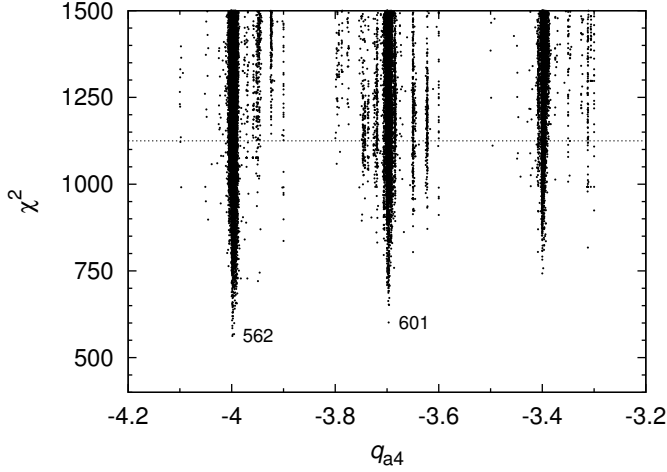


Figure 6: The values of χ^2 for all simulations of collisional evolution as function of the parameter q_{a4} (i.e. the slope of the SFD of the outer belt for asteroids with diameters $D \gtrsim 100$ km). The two marked values $\chi^2 = 562$ and 601 are statistically equivalent, but as we can see, more statistically-equivalent results correspond to the value of $q_{a4} \approx -4.0$.

best initial slopes q_{a1-6} and q_{c1-6} are both steeper and they exceed the value -3.5 derived by Dohnanyi. The SFD of the Cybele zone is significantly flatter than the SFDs of the other populations.

6.2. A detailed analysis of the parameters space

We also tried to explore the parameter space in detail — with smaller changes of input parameters between cycles and also smaller steps of the simplex. The best χ^2 which we found is however statistically equivalent to the previous value and we did not obtain a significant improvement of the SFDs. Parameters are not well-constrained in this limited parameter space, because the simulations were performed in a close surroundings of a local minimum and the simplex was mostly contracting. An even more-detailed exploration of the parameter space thus would not lead to any improvement and we decided to proceed with a model for rubble-pile asteroids.

7. Simulations for rubble-pile objects

The material characteristics of asteroids can significantly influence their mutual collisions. We can modify the Boulder code for rubble-pile bodies on the basis of Benavidez et al. (2012) work, who ran a set of SPH simulation for rubble-pile $D_{PB} = 100$ km parent bodies. **We used data from their Fig. 8, namely diameters of fragments inferred for simulations with various projectile diameters and impact velocities.**

7.1. Modifications of the Boulder code for rubble-pile bodies

We need to modify the parameters of the scaling law first. For the density of asteroids, we used $\rho = 1.84$ g/cm³ as Benavidez et al. (2012). We determined the specific impact energy Q_D^* required to disperse half of the total mass of a $D = 100$ km

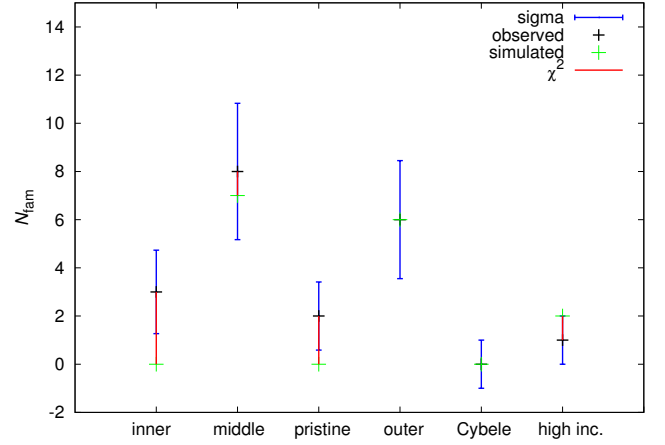


Figure 8: The differences between simulated and observed numbers of families N_{fam} in individual populations, corresponding to $\chi^2 = 562$. Sigma denotes the uncertainty of the observed number of families. The results of simulations with monoliths. The simulated and observed numbers of families are consistent within the uncertainties.

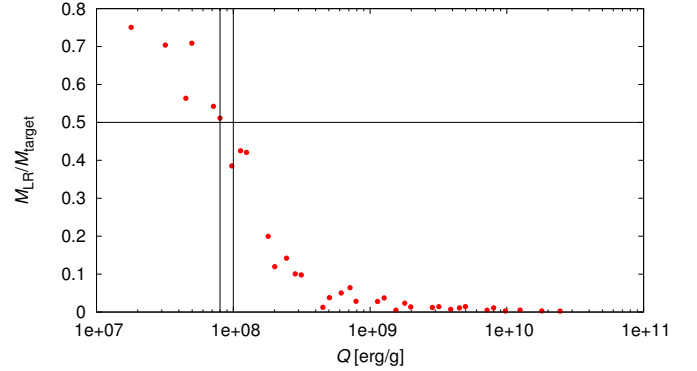


Figure 9: The dependence of the mass of the largest remnant M_{LR} on the kinetic energy Q of the projectile for rubble-pile bodies. We mark with lines: the value $M_{LR}/M_{target} = 0.5$, according to this value we determine Q_D^* ; the uncertainties of the determination of Q_D^* . **The result is $Q_D^* = (9 \pm 1) \times 10^7$ erg/g.**

rubble-pile target from the dependence of the mass of the largest remnant M_{LR} as a function of the kinetic energy of projectile

$$Q = \frac{\frac{1}{2} M_{projectile} v_{imp}^2}{M_{tot}}, \quad (4)$$

where $M_{tot} = M_{target} + M_{projectile}$ (see Figure 9). Q_D^* is then equal to Q corresponding to $M_{LR}/M_{target} = 0.5$. So the result is $Q_D^* = (9 \pm 1) \times 10^7$ erg/g and the corresponding parameter q_{fact} in the scaling law is then 13.2 ± 1.5 (**calculated according to Eq. (2) with $\rho = 1.84$ g/cm³, $r = 5 \times 10^6$ cm, parameters Q_0 , a , B and b remain same as for the monolithic bodies**). The scaling law for rubble-pile bodies was already shown graphically in Figure 4.

We must also derive new dependencies of the slope $q(Q)$ of the fragments' SFD and for the mass of the largest fragment $M_{LF}(Q)$ on the specific energy Q of the impact. The cumulative SFDs of the fragments cannot be always described with only a single slope. We thus divided the fragments according to their

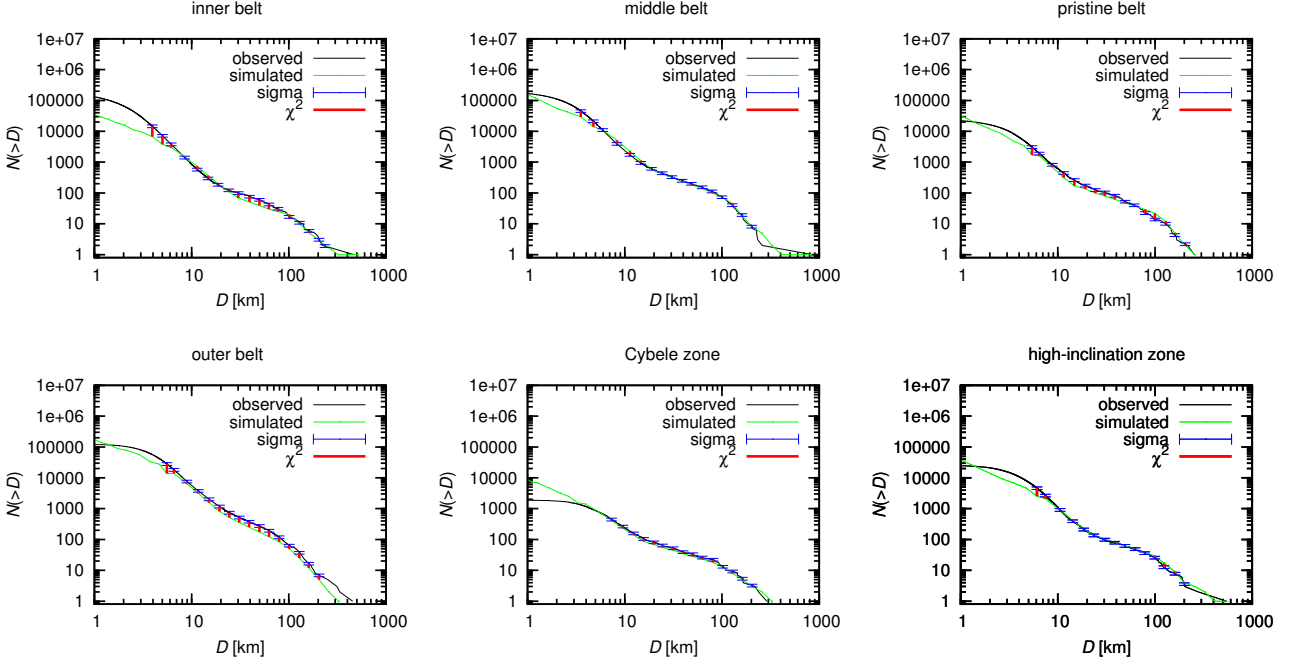


Figure 7: The observed (black line) and simulated (green line) SFDs and the differences between them for the simulation with $\chi^2 = 562$. Sigma denotes the (prescribed) uncertainty of the observed SFD. This result is for the simulation with monoliths. The largest differences are for the inner and outer belt.

Table 6: The parameters describing the initial SFDs (for time $t = -4$ Gyr) of the six parts of the main belt for which we obtained the best fits of the observed SFDs ($\chi^2 = 562$). d_1 , d_2 , q_a , q_b , q_c and n_{norm} denote the same parameters as in Table 4 and are rounded to two decimal places.

population	d_1 (km)	d_2 (km)	q_a	q_b	q_c	n_{norm}
inner	90.07	20.03	-4.20	-2.10	-4.20	20.03
middle	105.07	18.03	-4.60	-2.30	-4.20	75.07
pristine	100.07	13.03	-3.90	-2.30	-4.20	21.03
outer	80.07	20.03	-4.00	-2.50	-4.10	90.07
Cybele	80.07	15.03	-2.80	-2.00	-3.40	17.03
high-inclination	100.07	20.03	-4.20	-2.20	-4.10	30.03

diameters to small ($D < 10$ km) and large ($D > 10$ km) and we determined two slopes. Then we calculated the mean value and we used the differences between the two values as error bars (see Figure 10).

If a collision between asteroids is not energetic enough (i.e. a cratering), then only a little of the mass of the target is dispersed to the space. In this case, the largest body is called the *largest remnant*. The second largest body, which has a much lower mass, is called the *largest fragment*. If a collision is catastrophic, the first two fragments have comparable masses and in this case, the largest body is called the largest fragment. For some of the SPH simulations outcomes it can be difficult to determine the largest fragment. The error bars in Figure 11 correspond to the points, which we would get if we choose the other of the two above-mentioned possibilities as the largest fragment.

The parametric relations we determined for rubble-pile bodies are the following:

$$q(Q) = -6.3 + 3.16 \left(\frac{Q}{Q_D^*} \right)^{0.01} \exp \left(-0.008 \frac{Q}{Q_D^*} \right), \quad (5)$$

$$\frac{M_{LF}}{M_{tot}}(Q) = \frac{0.6}{13 \left(\frac{Q}{Q_b^*} \right)^{-1.2} + 1.5 \frac{Q}{Q_b^*}}. \quad (6)$$

When we approximate scattered data with functions, we must carefully check their limits — for decreasing impact energy we need M_{LF} to approach zero and the slope q staying negative and not increasing above 0. These conditions are the reasons why our functions do not go through all of the data points (not even within the range of uncertainties). This problem is most pronounced for the dependence of $M_{LF}(Q)$ for small Q (Figure 11). Nevertheless, we think that it is more important that the functions corresponds to the data for high Q 's, because highly-energetic collisions produce a lot of fragments and they influence the SFD much more significantly.

7.2. A comparison of results for monoliths and rubble-piles

We explored the parameter space in a similar way as for monoliths: with 729 different initial SFDs (i.e. 729 cycles), the maximum permitted number of iterations 300 and 218,700 simulations in total. The changes of parameters between cycles and the steps of the simplex within one cycle are same as for simulations with monolithic bodies (see Table 5).

The minimum χ^2 which we obtained was 1,321. The differences between the simulated and observed SFDs and the numbers of families for individual populations corresponding to $\chi^2 = 1,321$ are shown in Figures 12 and 13. These values are significantly higher than what we obtained for monoliths ($\chi^2 = 562$ at best). Given that the set of initial conditions was quite extensive (refer to Figure 5), we think that this difference is fundamental.

It seems that, at least within our collisional model, we can preliminarily conclude that the main belt does not contain *only* rubble-pile bodies, because otherwise the corresponding fit would not be that worse than for monoliths (see Figures 7 and 8 for a comparison).

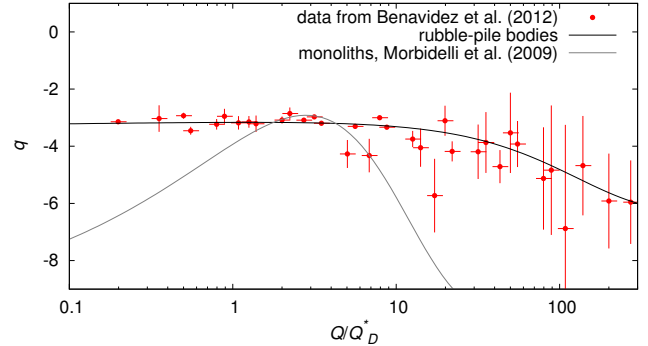


Figure 10: The slope q of the SFD of fragments as a function of the impact energy Q/Q_D^* for the rubble-pile parent bodies with $D_{PB} = 100$ km. The horizontal axis is in a logarithmic scale. The SFD of fragments is characterized by two slopes (for fragments $D < 10$ km and $D > 10$ km) and we calculated the mean value. The displayed uncertainties of q are the differences between real and mean values. The horizontal error bars are given by the uncertainties of Q_D^* . The grey line corresponds to the dependence for monoliths (Morbidelli et al., 2009), which we used in Section 6.

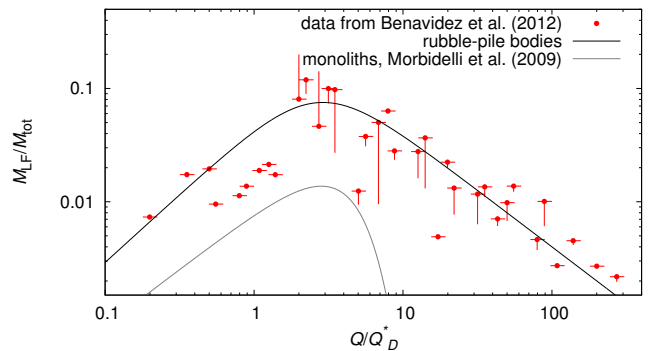


Figure 11: The ratio M_{LF}/M_{tot} (the mass of the largest fragment divided by the sum of the mass of target and the mass of projectile) as a function of the impact energy Q/Q_D^* for the rubble-pile parent bodies with the diameter $D_{PB} = 100$ km. The horizontal axis is in a logarithmic scale. The uncertainties of M_{LF}/M_{tot} are caused by a problematic determination of the largest fragment and the largest remnant. The horizontal error bars are given by the uncertainties of Q_D^* . The grey line corresponds to the dependence for monoliths (Morbidelli et al., 2009) **which we used in Section 6.**

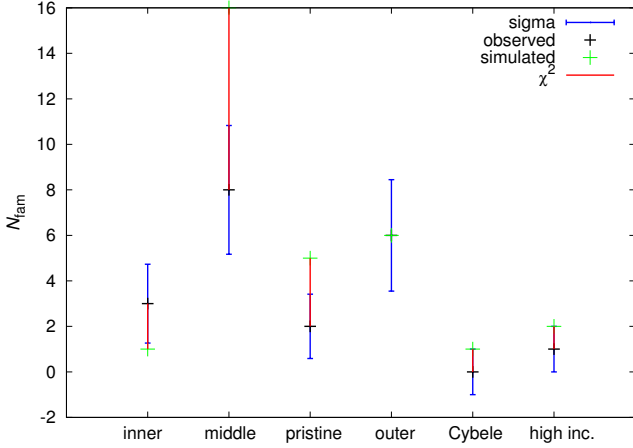


Figure 13: The simulated and the observed numbers of families N_{fam} in individual populations, corresponding to $\chi^2 = 1,321$. Sigma denotes the uncertainty of the observed number of families. The results from simulation with rubble-piles.

It would be interesting to run a simulation with two different population of the main belt — monolithic and rubble-pile bodies. Also because Benavidez et al. (2012) concluded that some asteroid families were more likely created by a disruption of a rubble-pile parent body: namely the Meliboea, Erigone, Misa, Agnia, Gefion and Rafita. Such simulation remains to be done.

8. Improvements and extensions of the model

We think that the match between our collisional model and the observational data as presented in Sections 6 and 7 is not entirely convincing. In this Section we thus try to improve the model by the following procedures: i) We use a longer ‘tail’ of the SFD (down to $D = 0.01$ km), which is a straightforward modification. Nevertheless, the longer tail means a significant increase of the required CPU time (which is proportional to N_{bins}^2). ii) We account for the Yarkovsky effect whose timescales for small bodies ($D \lesssim 0.1$ km) are already comparable to the collisional timescales (see Section 8.1). iii) We do not converge all 36 free parameters at once but we free only 6 of them (d_1 , d_2 , q_a , q_b , q_c and n_{norm} for one population only) and proceed sequentially with six parts of the main belt (see Section 8.2).

8.1. Dynamical decay caused by the Yarkovsky effect

In order to improve the Boulder code and use a more complete dynamical model, we try to account for the Yarkovsky effect as follows. We assume that the Yarkovsky effect causes a dynamical decay of the population which can be described by the following relation

$$N(t + \Delta t) = N(t) \exp\left(-\frac{\Delta t}{\tau_{\text{YE}}}\right), \quad (7)$$

where $N(t)$ denotes the number of bodies at time t , Δt the time step of the integrator and τ_{YE} is the characteristic timescale.

Table 7: The parameters of the Yarkovsky-driven decay which are dependent on the zone of the main asteroid belt: Δa is half of the zone size (or a typical distance from neighbouring strong mean-motion resonances), ρ denotes the (bulk and surface) density assumed for respective bodies.

zone	Δa AU	ρ kg m ⁻³
inner	0.2	2,500
middle	0.1615	2,500
pristine	0.0665	1,300
outer	0.162	1,300
Cybele	0.105	1,300
high- I	0.135	1,300

We can compute the semimajor-axis drift rate da/dt , for both the diurnal and seasonal variants of the Yarkovsky effect, using the theory of Vokrouhlický (1998), Vokrouhlický and Farinella (1999) and the (size-dependent) time scale is then

$$\tau_{\text{YE}}(D) = \frac{\Delta a}{da/dt(D)}, \quad (8)$$

where Δa is the range of semimajor axis given by the positions of major mean-motion resonances which are capable to remove objects from the respective populations. It differs for different zones of the main belt, of course (see Table 7).

In the thermal model, we assume the following parameters: the thermal conductivity $K = 0.01$ W m⁻¹ K⁻¹ for $D > D_{\text{YE}}$, i.e. a transition diameter, and 1.0 W m⁻¹ K⁻¹ for $D \leq D_{\text{YE}}$, thermal capacity $C = 680$ J kg⁻¹ K⁻¹, Bond albedo $A = 0.02$, infrared emissivity $\epsilon = 0.95$. Remaining thermal parameters, namely the densities, are summarized in Table 7.

We tested five different models (assumptions):

1. low thermal conductivity $K = 0.01$ W m⁻¹ K⁻¹ only, i.e. $D_{\text{YE}} = 0$ km, fixed rotation period $P = 5$ h;
2. both low/high K with $D_{\text{YE}} = 200$ m, again $P = 5$ h;
3. the same $K(D)$ dependence, but size-dependent spin rate $\omega(D) = \frac{2\pi}{P_0} \frac{D_0}{D}$, $P_0 = 5$ hour, $D_0 = 5$ km;
4. $\omega(D) = \frac{2\pi}{P_0} \left(\frac{D}{D_0}\right)^{-1.5}$, $P_0 = 2$ h, $D_0 = 0.2$ km (see Figure 14);
5. we used Bottke et al. (2005) time scales.

We then computed the Yarkovsky timescales $\tau_{\text{YE}}(D)$ (Figure 15) and constructed a ‘testing’ collisional model in order to check the influence of the dynamical decay on the evolution of the main belt SFD. Note that for small sizes $D \lesssim 1$ km, $\tau_{\text{YE}}(D)$ can be even smaller than corresponding collisional timescales $\tau_{\text{col}}(D)$.

The results of models 1 and 2 are clearly not consistent with the observed SFD (see Figure 16). The results of 3, 4 and 5 seem to be equivalent and consistent with observations, however, we cannot distinguish between them. We can thus exclude ‘extreme’ Yarkovsky drift rates and conclude that only lower or ‘reasonable’ drift rates provide a reasonable fit to the observed SFD of the main belt.

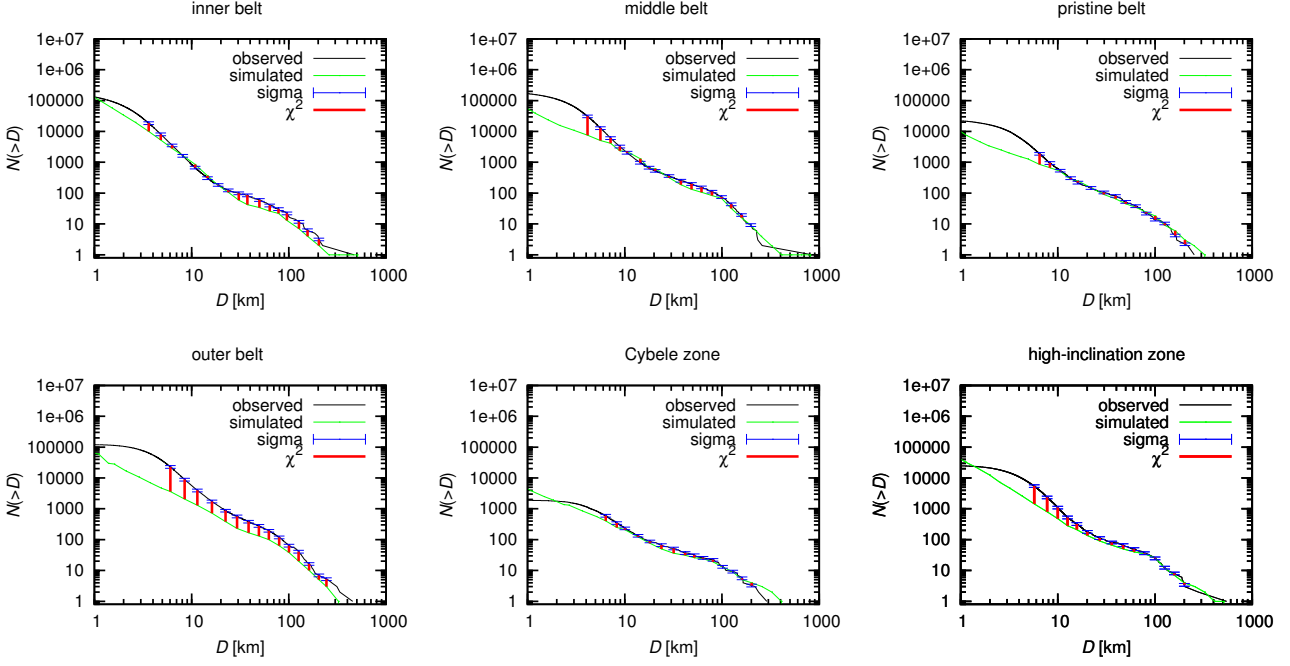


Figure 12: The observed (black line) and simulated (green line) SFDs and the differences between them for the simulation with total $\chi^2 = 1,321$. Sigma denotes the adopted uncertainty of the observed SFD. The results from simulation with rubble-piles.

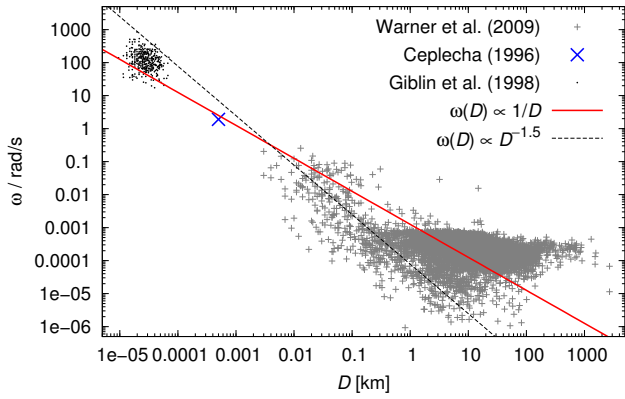


Figure 14: The spin rate ω vs size D dependent for asteroids (observational data from Warner et al., 2009), the Lost City fireball (Ceplecha, 1996) and fragments in laboratory experiments (Giblin et al., 1998). Two approximations are given: $\omega(D) \propto 1/D$, and $\omega(D) \propto D^{-1.5}$, which better fits the observational data in the size range $D \in (0.01, 1)$ km where the Yarkovsky drift is the most important with respect to the collisional model. Nevertheless, we cannot yet exclude a possibility that the observed $\omega(D)$ distribution is still strongly biased for small $D \lesssim 1$ km.

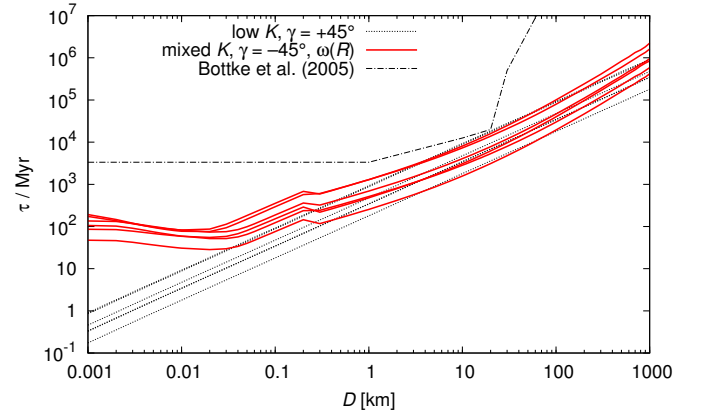


Figure 15: The timescale τ_{YE} of the Yarkovsky-driven decay vs size D for three different models (denoted 1, 3 and 5), or in other words, assumptions on the thermal conductivity $K(D)$ and the spin rate $\omega(D)$, which were described in the text. Model 2 is quite similar to 1 and model 4 is similar to 3, so we decided not to plot them in order to prevent many overlapping lines. For each model, we plot six lines corresponding to the six zones of the main belt: inner, middle, ‘pristine’, outer, Cybele and high- I . Bottke et al. (2005) time scales were used for the whole main belt (regarded as a single population).

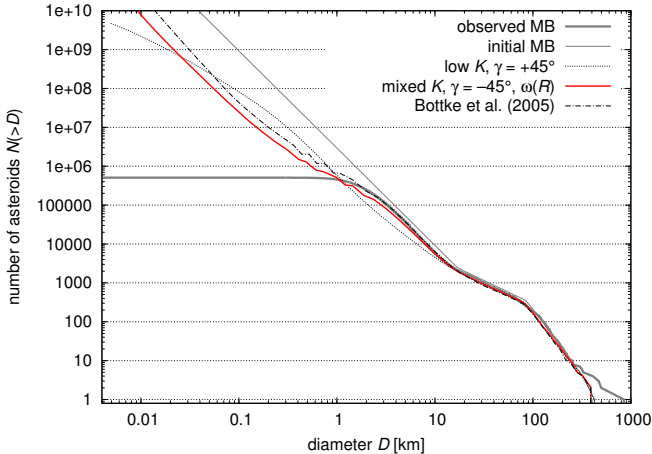


Figure 16: Resulting synthetic size-frequency distributions of the main belt (regarded as a single population) after 4 Gyr of collisional evolution, as computed by the Boulder code. We show results for three different models of the Yarkovsky-driven decay (denoted 1, 3 and 5 in the text). Model 1 (dotted line) is clearly inconsistent with the observed SFD (thick gray line).

8.2. Subsequent fits for individual parts of the main belt

In order to improve our ‘best’ fit from Section 6 (and 7), we ran simplex sequentially six times, with only 6 parameters free in each case, namely d_1 , d_2 , q_a , q_b , q_c , n_{norm} for a given part of the main belt. We included a longer tail ($D_{\text{min}} = 0.01$ km) and the Yarkovsky model discussed above.⁹ The number of simplex iterations was always limited to 100.

We shall not be surprised if we obtain a χ^2 value which is (slightly) larger than before because we changed the collisional model and this way we moved away from the previously-found local minimum. At the same time, we do not perform that many iterations as before (600 vs. 218,700), so we cannot ‘pick-up’ the deepest local minima.

For monoliths, we tried to improve the ‘best’ fit with $\chi^2 = 562$. However, the initial value at the very start of the simplex was $\chi^{2'} \approx 803$ (due to the changes in the collisional model) and the final value after the six subsequent fits $\chi^{2''} = 520$. This is only slightly smaller than the previous χ^2 and statistically equivalent ($\chi^{2''} \approx \chi^2$). We interpret this as follows: our simplex algorithm naturally selects deep local minima. It seems that the lowest χ^2 (for a given set of initial conditions) can be achieved by a ‘lucky’ sequence of disruptions of relatively large bodies ($D_{\text{PB}} \gtrsim 100$ km) which results in synthetic SFD’s and the numbers of families best matching the observed properties. Of course, this sequence depends on the ‘seed’ value of the random-number generator.

To conclude, our improvements of the collisional model do not seem significant and the χ^2 values are of the same order. This can be considered as an indication that we should

⁹This more complicated model runs about 10 times slower, because we have both larger number of bins to account for smaller bodies and a shorter time step to account for their fast dynamical removal. It is thus not easy to run a whole set of simulations from Sections 6 and 7 again.

probably use an even more complicated model. (Nevertheless, there is still a significant difference between monoliths and rubble-piles and the assumption of monolithic structure matches the observations better.)

8.3. Simulations with various scaling laws

So far we used the scaling law of Benz and Asphaug (1999) for all simulations. In this Section, we are going to test different scaling laws. Similarly as Bottke et al. (2005), we changed the specific impact energy Q_D^* of asteroids with $D > 200$ m (see Figure 17, left). For each scaling law we ran 100 simulations of the collisional evolution with different random seeds. The initial parameters of SFDs are fixed and correspond to the best-fit initial parameters found in Section 6.

In order to decide which scaling laws are suitable, we can simply compare the resulting synthetic SFDs and the numbers of families to the observed ones. It is clear that if we increase the strength of $D \approx 100$ km bodies by a factor of 10 or more, the number of synthetic families (namely catastrophic disruptions with $D_{\text{PB}} \geq 100$ km) is much smaller than the observed number (usually 4 vs 20, see in Figure 17, middle). On the other hand, if we decrease the strength by a factor of 10, the synthetic SFDs exhibit a significant deficit of small bodies with $D < 10$ km due to a collisional cascade (especially in the inner belt, see Figure 17, right). Moreover, the number of synthetic families is then significantly larger, of course.

These results lead us to the conclusion, that the ‘extreme’ scaling laws (i.e. much different from Benz and Asphaug 1999) cannot be used for the main asteroid belt. This result is also in accord with Bottke et al. (2005).

9. Conclusions

In this work, we created a new collisional model of the evolution of the main asteroid belt. We divided the main belt to six parts and constructed the size-frequency distribution for each part. The observed SFDs differ significantly in terms slopes and total numbers of asteroids. We then ran two sets of simulations — for monolithic bodies and for rubble-pile.

In the case of monoliths, there seem to be (relatively minor) discrepancies between the simulated and observed SFD’s in individual parts of the main belt, nevertheless, the numbers of families (catastrophic disruptions) correspond within uncertainties. On the other hand, the χ^2 value for rubble-pile bodies is more than twice as large because there are systematic differences between the SFD’s and the (mean) number of rubble-pile families is substantially larger (usually 30 or more) than the observed ones (20 in total). We can thus conclude that within our collisional model, monolithic asteroids provide a better match to the observed data than rubble-piles, even though we cannot exclude a possibility that a certain part of the population is indeed of rubble-pile structure, of course.

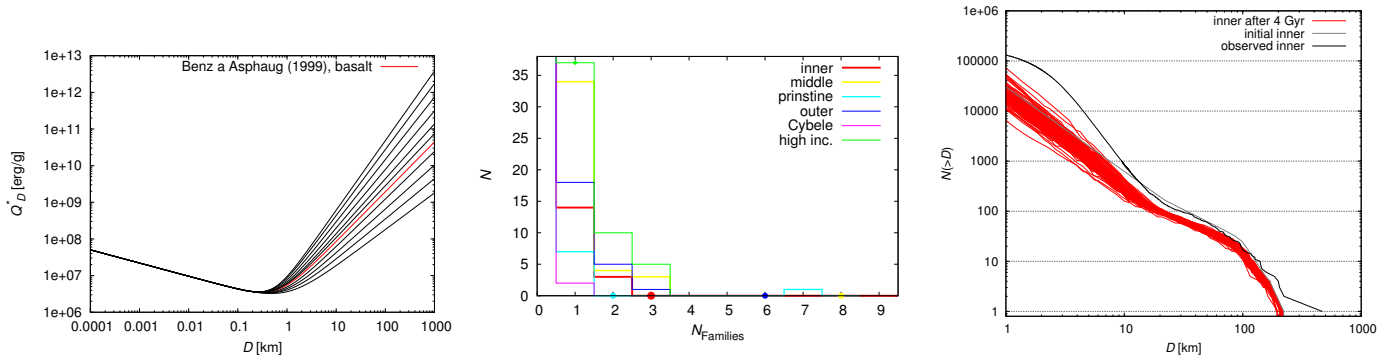


Figure 17: Left: scaling laws with different firmness of large bodies. The red line represents the scaling law of Benz and Asphaug (1999). Middle: histogram representing in how many simulations (of 100) was created a given number of families N_{families} for the scaling law with the increased firmness of large bodies. The observed numbers of families are displayed with points. Right: The final SFD of the inner belt for the scaling law with the decreased firmness of large bodies. All 100 simulations are displayed.

We tried to improve our model by: (i) introducing a longer ‘tail’ of the SFD (down to $D = 0.01$ km;¹⁰ (ii) incorporating the Yarkovsky effect, i.e. a size-dependent dynamical decay; (iii) running many simulations with different random seeds, in order to find even low-probability scenarios. Neither of these improvements provided a substantially better match in *all* parts of the main belt at once.

However, we can think of several other possible reasons, why the match between our collisional model and the observed SFD’s is not perfect:

1. There are indeed different scaling laws for different parts of the main belt. This topic is a natural continuation of our work (and a detailed analysis is postponed to a forthcoming paper).
2. The scaling of the SPH simulations from $D_{\text{PB}} = 100$ km by one or even two orders of magnitude is likely problematic. Our work is thus a motivation to study disruptions of both smaller ($D_{\text{PB}} \approx 1$ km) and larger (400 km) targets. Similar sets of SPH simulations as in Durda et al. (2007) and Benavidez et al. (2012) would be very useful for further work.
3. To explain the SFD of the inner belt, namely its ‘tail’, we would need to assume a recent disruption (during the last ~ 100 Myr) of a large parent body ($D_{\text{PB}} \gtrsim 200$ km). On the other hand, there must not have occurred a recent large disruption in the middle or the outer belt, otherwise the synthetic SFD is more populous than the observed one. It is not likely, that all such conditions are fulfilled together in our model, in which collisions occur randomly.
4. When we split the main belt into 6 parts, the evolution seems too stochastic (the number of large events in individual part is of the order of 1). It may be even useful to prepare a ‘deterministic model’, in which large disruptions are *prescribed*, according to the observed families and their ages. Of course, the completeness of the family list and negligible bias are then crucial.

¹⁰Plus the so-called ‘negative’ (invisible) tail implemented in the Boulder code to prevent artificial waves on the SFD.

5. We can improve the modelling of the Yarkovsky/YORP effect, e.g. assume a more realistic distribution of spin rates (not only the $\omega(D)$ dependence, Figure 14) and perform an N -body simulation of the orbital evolution to get a more accurate estimate of the (exponential) time scale $\tau_{\text{YE}}(D)$. It may be difficult to estimate biases in the $\omega(D)$ plot, because the dataset is heterogeneous.
6. Maybe, the intrinsic collisional probabilities p_i were substantially different (lower) in the past, e.g. before major asteroid families were created.
7. Some of the mutual impact velocities v_{imp} , especially with high-inclination objects, are substantially larger than the nominal 5 km s^{-1} , so the outcomes of these collisions are most-likely different. On the other hand, these collisions are usually of lower probability and the high-inclination region is not that populous, so that this effect has likely a minor contribution only.
8. There might be several large undiscovered families, or in other words, the lists of $D_{\text{PB}} \leq 100$ km families (Brož et al., 2013, or Masiero et al., 2013) might be strongly biased, because comminution is capable to destroy most of the fragments.¹¹
9. Possibly, parent-body sizes D_{PB} of the observed families are systematically underestimated or their mass ratios $M_{\text{LR}}/M_{\text{PB}}$ of the largest remnant to parent body are offset, even though they were determined by best available methods (Durda et al. 2007, Tanga et al. 1999).

The topics outlined above seem to be good starting points for (a lot of) further work.

Acknowledgements

The work of MB has been supported by the Grant Agency of the Czech Republic (grant no. 13-01308S) and the Research

¹¹It seems that the late heavy bombardment is indeed capable to destroy $D_{\text{PB}} \leq 100$ km families, as concluded by Brož et al. (2013), but in this paper we focus on the last ~ 4 Gyr only and we do not simulate the LHB.

Programme MSM0021620860 of the Czech Ministry of Education. We thank also to Alessandro Morbidelli for valuable discussions on the subject and William F. Bottke for a computer code suitable for computations of collisional probabilities.

References

- Benavidez, P. G., Durda, D. D., Enke, B. L., Bottke, W. F., Nesvorný, D., Richardson, D. C., Asphaug, E., Merline, W. J., May 2012. A comparison between rubble-pile and monolithic targets in impact simulations: Application to asteroid satellites and family size distributions. *Icarus* 219, 57–76.
- Benz, W., Asphaug, E., Nov. 1999. Catastrophic Disruptions Revisited. *Icarus* 142, 5–20.
- Bottke, W. F., Durda, D. D., Nesvorný, D., Jedicke, R., Morbidelli, A., Vokrouhlický, D., Levison, H., May 2005. The fossilized size distribution of the main asteroid belt. *Icarus* 175, 111–140.
- Bottke, W. F., Greenberg, R., May 1993. Asteroidal collision probabilities. *Geophys. Res. Lett.* 20, 879–881.
- Bottke, W. F., Morbidelli, A., Jedicke, R., Petit, J.-M., Levison, H. F., Michel, P., Metcalfe, T. S., Apr. 2002. Debaised Orbital and Absolute Magnitude Distribution of the Near-Earth Objects. *Icarus* 156, 399–433.
- Bottke, Jr., W. F., Vokrouhlický, D., Rubincam, D. P., Nesvorný, D., May 2006. The Yarkovsky and Yorp Effects: Implications for Asteroid Dynamics. *Annual Review of Earth and Planetary Sciences* 34, 157–191.
- Bowell, E., Hapke, B., Domingue, D., Lumme, K., Peltoniemi, J., Harris, A. W., 1989. Application of photometric models to asteroids. In: Binzel, R. P., Gehrels, T., Matthews, M. S. (Eds.), *Asteroids II*. pp. 524–556.
- Brož, M., Morbidelli, A., Bottke, W. F., Rozehnal, J., Vokrouhlický, D., Nesvorný, D., Mar. 2013. Constraining the cometary flux through the asteroid belt during the late heavy bombardment. *Astron. Astrophys.* 551, A117.
- Cepplecha, Z., Jul. 1996. Luminous efficiency based on photographic observations of the Lost City fireball and implications for the influx of interplanetary bodies onto Earth. *Astron. Astrophys.* 311, 329–332.
- Dahlgren, M., Aug. 1998. A study of Hilda asteroids. III. Collision velocities and collision frequencies of Hilda asteroids. *Astron. Astrophys.* 336, 1056–1064.
- Davis, D. R., Chapman, C. R., Greenberg, R., Weidenschilling, S. J., Harris, A. W., 1979. Collisional evolution of asteroids - Populations, rotations, and velocities. pp. 528–557.
- Dohnanyi, J. S., May 1969. Collisional Model of Asteroids and Their Debris. *J. Geophys. Res.* 74, 2531.
- Durda, D. D., Bottke, W. F., Nesvorný, D., Enke, B. L., Merline, W. J., Asphaug, E., Richardson, D. C., Feb. 2007. Size-frequency distributions of fragments from SPH/N-body simulations of asteroid impacts: Comparison with observed asteroid families. *Icarus* 186, 498–516.
- Giblin, I., Martelli, G., Farinella, P., Paolicchi, P., di Martino, M., Smith, P. N., Jul. 1998. The Properties of Fragments from Catastrophic Disruption Events. *Icarus* 134, 77–112.
- Greenberg, R., Jan. 1982. Orbital interactions - A new geometrical formalism. *Astron. J.* 87, 184–195.
- Hodapp, K. W., Kaiser, N., Aussel, H., Burgett, W., Chambers, K. C., Chun, M., Dombek, T., Douglas, A., Hafner, D., Heasley, J., Hoblitt, J., Hude, C., Isani, S., Jedicke, R., Jewitt, D., Laux, U., Luppino, G. A., Lupton, R., Maberry, M., Magnier, E., Mannery, E., Monet, D., Morgan, J., Onaka, P., Price, P., Ryan, A., Siegmund, W., Szapudi, I., Tonry, J., Wainscoat, R., Waterson, M., Oct. 2004. Design of the Pan-STARRS telescopes. *Astronomische Nachrichten* 325, 636–642.
- Knežević, Z., Milani, A., Jun. 2003. Proper element catalogs and asteroid families. *Astron. Astrophys.* 403, 1165–1173.
- Masiero, J. R., Mainzer, A. K., Bauer, J. M., Grav, T., Nugent, C. R., Stevenson, R., Jun. 2013. Asteroid Family Identification Using the Hierarchical Clustering Method and WISE/NEOWISE Physical Properties. *Astrophys. J.* 770, 7.
- Masiero, J. R., Mainzer, A. K., Grav, T., Bauer, J. M., Cutri, R. M., Dailey, J., Eisenhardt, P. R. M., McMillan, R. S., Spahr, T. B., Skrutskie, M. F., Tholen, D., Walker, R. G., Wright, E. L., DeBaun, E., Elsbury, D., Gautier, IV, T., Gomillion, S., Wilkins, A., Nov. 2011. Main Belt Asteroids with WISE/NEOWISE. I. Preliminary Albedos and Diameters. *Astrophys. J.* 741, 68.
- Michel, P., Jutzi, M., Richardson, D. C., Benz, W., Jan. 2011. The Asteroid Veritas: An intruder in a family named after it? *Icarus* 211, 535–545.
- Morbidelli, A., Bottke, W. F., Nesvorný, D., Levison, H. F., Dec. 2009. Asteroids were born big. *Icarus* 204, 558–573.
- Nesvorný, D., Nov. 2010. Nesvorný HCM Asteroid Families V1.0. NASA Planetary Data System 133.
- Nesvorný, D., Jedicke, R., Whiteley, R. J., Ivezić, Ž., Jan. 2005. Evidence for asteroid space weathering from the Sloan Digital Sky Survey. *Icarus* 173, 132–152.
- Press, W. H., Teukolsky, S. A., Vetterling, W. T., Flannery, B. P., 1992. Numerical recipes in FORTRAN. The art of scientific computing.
- Stuart, J. S., Nov. 2001. A Near-Earth Asteroid Population Estimate from the LINEAR Survey. *Science* 294, 1691–1693.
- Tanga, P., Cellino, A., Michel, P., Zappalà, V., Paolicchi, P., dell’Oro, A., Sep. 1999. On the Size Distribution of Asteroid Families: The Role of Geometry. *Icarus* 141, 65–78.
- Tedesco, E. F., Noah, P. V., Noah, M., Price, S. D., Feb. 2002. The Supplemental IRAS Minor Planet Survey. *Astron. J.* 123, 1056–1085.
- Vokrouhlický, D., Jul. 1998. Diurnal Yarkovsky effect as a source of mobility of meter-sized asteroidal fragments. I. Linear theory. *Astron. Astrophys.* 335, 1093–1100.
- Vokrouhlický, D., Farinella, P., Dec. 1999. The Yarkovsky Seasonal Effect on Asteroidal Fragments: A Nonlinearized Theory for Spherical Bodies. *Astron. J.* 118, 3049–3060.
- Walsh, K. J., Delbó, M., Bottke, W. F., Vokrouhlický, D., Lauretta, D. S., Jul. 2013. Introducing the Eulalia and new Polana asteroid families: Re-assessing primitive asteroid families in the inner Main Belt. *Icarus* 225, 283–297.
- Warner, B. D., Harris, A. W., Pravec, P., Jul. 2009. The asteroid lightcurve database. *Icarus* 202, 134–146.
- Zappalà, V., Bendjoya, P., Cellino, A., Farinella, P., Froeschlé, C., Aug. 1995. Asteroid families: Search of a 12,487-asteroid sample using two different clustering techniques. *Icarus* 116, 291–314.